Short Communication

The Effect of Thermal Inputs on Microstructure and Corrosion Resistance of WC Particle-Reinforced High Chromium Wear-Resistant Steel

Ben Niu[1], Junfu Chen[1,], Yaoyong Yi[1], Linlin Pan[1], Xiaodong Zou[1], Jianglong Yi[1], Yongjun Hu[2]*

[1] Guangdong Provincial Key Laboratory of Advanced Welding Technology, China-Ukraine Institute of Welding, Guangdong Academy of Sciences (China-Ukraine E. O. Paton Institute of Welding), Guangzhou, Guangdong, 510650, P.R. China;
[2] Guangdong University of Technology, Guangzhou 510006, P.R. China.
*E-mail: niub@gwi.gd.cn

The purpose of this study is to improve corrosion resistance of WC particle reinforced high-chromium wear-resistant steel by different thermal inputs. The polarization curve and electrochemical impedance spectroscopy of the sample at a low potential in 3.5% NaCl solution were studied by using an electrochemical workstation. Electrochemical changes in the region near the fusion line were examined by scanning vibrating electrode technique (SVET). Micro morphology was explored via an optical microscope (OM). The electrochemical results show that corrosion resistance initially increases and then decreases with increasing thermal inputs. Sample #2 displayed the highest corrosion potential (-0.491 V) and the lowest corrosion current density (3.78×10^{-4} μA·cm^2) of all the conditions. The SVET results and microstructure imply that the excellent electrochemical performance of high-chromium wear-resistant steel is attributed to the reasonably well thermal inputs, which can both provide efficient elemental distribution and promote the dissolution of the WC phase. This work provides new insight into the improvement of corrosion resistance of high-chromium wear-resistant steel.

1. INTRODUCTION

In recent years, wear-resistant material has become a growing field, garnering an increasing amount of interest and research [1, 2]. High-chromium wear-resistant steels are promising candidates for application in mining machinery due to their outstanding abrasion resistance and superior thermal shock resistance [3, 4]. However, the erosion of high content chromium wear resistant steel is inevitable

Int. J. Electrochem. Sci., 16 (**2021**) Article ID: 210766

2

due to the electrical potential difference between precipitates [5]. Furthermore, the high temperature and high-pressure service environments also lead to rapid failure of the weld interface [6]. These drawbacks limit the further application of high-chromium wear resistant steel in machinery [7].

To address this limitation, a great deal of research has been carried out. This research includes element doping, surface modification and anticorrosion coating. In particular detail, Viswanathan et al. [8] reported chromium-doped diamond-like carbon coatings on stainless steel. Their findings showed that the chromium doping enhanced the corrosion resistance of the stainless steel effectively. Ripoll et al. [9] indicated that Niobium concentrations of up to 3 wt% increased toughness and corrosion resistance in high-speed steel laser hard facings. At the same time, Liang et al. [10] explored the corrosion resistance of austenitic stainless steel after plasma nitriding, and found the corrosion performance was significantly improved. In addition, Xu et al. [11] described a set of studies that investigated a novel method for enhanced anticorrosion by graphene coating. The result suggested that as-grown graphene can protect material surfaces from oxidation in humid air lasting for more than 2.5 years. In summary, the corrosion resistance is strongly associated with the microstructure of high-chromium wear resistant steel.

To date, several physical and chemical strategy-based microstructures have been used to improve the corrosion resistance of high-chromium wear resistant steels. For example, Fossati et al. [12] pointed out that nitriding treatments performed at lower temperatures ($\leq$723 K) can distinctly increase the corrosion resistance properties due to the avoidance of large CrN precipitation. Tang et al. [13] demonstrated that the corrosion resistance of these high-chromium alloys mainly depended on the Cr concentrations in the matrix and the volume fraction of carbides. Bartkowski et al. [14] presented the study results of metal matrix composite coatings (MMC coating) in a system of Stellite-6 and tungsten carbides. The above research provides an important basis and reference to improve the corrosion resistance of high-chromium wear resistant steel, although not completely satisfactorily. On one hand, it is difficult to control the corrosion resistance of high-chromium wear resistant steel [15]. On the other hand, the coordination mechanism of corrosion resistance of various elements has remained elusive [16]. Therefore, it is necessary and challenging to develop a corrosion improvement strategy for high-chromium wear resistant steel.

In this study, thermal inputs are proposed to improve the microstructure and corrosion resistance in WC particle-reinforced high-chromium wear-resistant steel. Impedance and Tafel curves were used to evaluate the electrochemical corrosion ability under different thermal input conditions. Furthermore, the microstructural and electrochemical changes in the region near the fusion line have been used to elucidate the association between corrosion resistance and microstructure in high-chromium wear resistant steel. The corrosion mechanisms of different structures of high-chromium wear resistant steel are preliminarily revealed. The results can provide a theoretical reference for improving the corrosion resistance of high-chromium wear-resistant steel.

2. EXPERIMENTAL DETAIL

2.1 Preparation of surface coating

The required flux core wire was prepared by flux cored wire XZ-YCX8 production equipment (Tianjin Xuzhi Co., Ltd.). The flux cored wire is formed by cold steel strip forming method. The steel strip with a certain width is transformed from a plane state to a "U" shape with uniform thickness after rolling deformation. The powder is added to the "U" groove, and then the "O" shape is formed after multiple rolling sealing. The finished welding wire is obtained through the drawing process including rough drawing and fine drawing (WC 20 wt. %, Cr 10 wt.%, Ni 13wt. %, Mn-Fe 5wt. %, Si-Fe 3 wt.%, Bal. Fe) the filling rate was 30% and the diameter of welding wire was Φ 1.6 mm). ZGCr17Mo2 steel plate was used as a base material for surface welding, and its composition is shown in Table 1. A double layer surfacing test was carried out by using an inverter welding machine (Phoenix 521 forcearc puls DW) and pure argon as the shielding gas (the argon flow rate is 60 L/3600 s). The welding parameters are shown in Table 2.

Table 1. Composition of ZGCr17Mo2 (wt.%)

C	Mn	Cr	Mo	Si	S	P	Fe
1.20	0.70	17.03	1.62	0.56	≤0.04	0.04	Bal.

Table 2. Process parameters of gas shielded flux cored wire arc surfacing

Samples	Welding current（A）	Voltage（V）	Welding speed（m/h）	thermal input kJ/cm
1#	247	22	12.9	88.46
2#	263	25.2	14.7	91.30
3#	291	27.6	15.6	104.26

Due to the existence of oil and other impurities on the surface of the base metal, the welding plate needs to be pretreated before the implementation of surfacing welding. Firstly, the oil stain on the surface is cleaned with acetone. Then the rust and oxide scale are removed by a grinding machine. During surface welding, the lap ratio of the same layer should be about 1/3 [18]. In the welding process, the included angles between the electrode and the horizontal plate and the welding direction are 45 degrees and 65 degrees respectively, and the straight-line strip transportation method is adopted. Air cooling to room temperature after welding. The schematic diagram of surface welding is shown in Figure 1.

Int. J. Electrochem. Sci., 16 (**2021**) Article ID: 210766

4
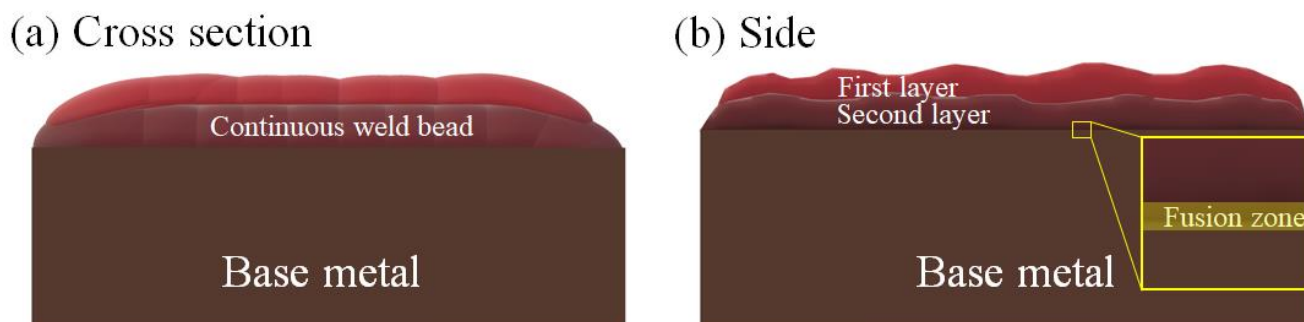
Figure 1. The schematic diagram of surface welding

*2.2 Materials characterization and electrochemical measurements*

The specimens were cut radially along the welding layer, and size is 20 mm × 20 mm × 30 mm. Before corrosion with an aqua regia solution to the sample for 5 s, mechanical water grinding and polishing were performed. The microstructure and distribution of WC were observed by a Leica dm-irm metallographic microscope. The polarization curve, open circuit potential, and impedance of surfacing layer were measured at an electrochemical workstation.

Meanwhile, the corrosion potential of the surfacing layer was measured by a powdll converter micro area electrochemical workstation. The electrochemical impedance spectroscopy (EIS) and SVET test after a 30-min immersion within 3.5 wt.% NaCl aqueous solution. A three-electrode system was employed (10 mm × 10 mm samples), a saturated calomel electrode and a platinum electrode were used as the working electrodes, reference electrode and auxiliary electrode, respectively. The electrochemical workstation (GAMRY Interface 1010) and the VersaSCAN electrochemical scanning system (AMETEK, VersaSCAN) were thereafter employed to examine the electrochemical behaviors of the above. Potentiodynamic curves were recorded at a scanning rate of -1 mV/s from -0.3 V to 0.3 V at 25°C. The electrochemical impedance spectroscopy (EIS) measurements were set under the open circuit potential (OCP) at a frequency of 0.01 Hz~100 KHz, as well as an AC drive signal amplitude of 1 mV/s. An SVET test was performed on samples with dimensions of 3 mm × 3 mm region. The Pt-Ir probe was placed above the sample surface and the height was controlled between 100 μm-120 μm using a video camera. The SVET measurements were conducted under the OCP, with the vibrating amplitude and vibrating frequency of the micro-probe of 30 μm and 80 Hz, respectively.

3. RESULTS AND DISCUSSION

3.1 Microstructure of surfacing layer

The microstructural of the surface layer are shown in Figure 2. The WC-reinforced high-chromium surface layer is mainly composed of austenite and eutectic carbide, in which the austenite matrix is dendrite and the eutectic carbide is a network structure.
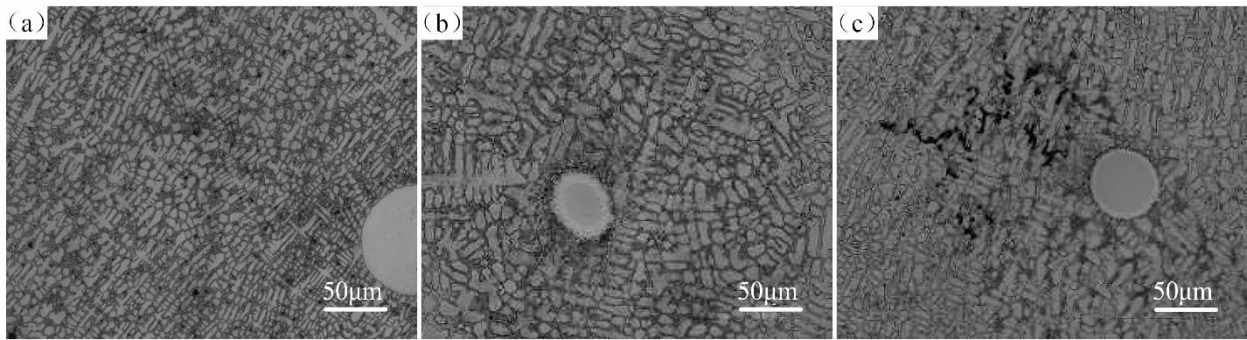
Figure 2. Microstructure of the top area of the surface layer with different thermal inputs (a) 1# (b) 2# and (c) 3#.

It can be seen from Figure 2a that the carbide particles in the sample are large, about 150 μm. The area of austenite and eutectic carbide accounts for 46.04% and 53.96%, respectively (grain size of grade 10). With the increase of heat input, the diameter of the WC particles decreases and an obvious melting phenomenon appears (Figure 2b). The area of austenite and eutectic carbide accounted for 54.34% and 45.66%, respectively (grain size of grade 11) [19]. It should be noted that when the current increases to 290 A, the austenite dendrite is more obviously noticed (Figure 2c). The area of austenite and eutectic carbide accounts for 60.41 and 39.59%, respectively. The change in WC particle diameter is small and the austenite grain is refined with a grain size of grade 10. The above results indicate that there are less carbides precipitated in sample 2#.

3.2 Electrochemical properties
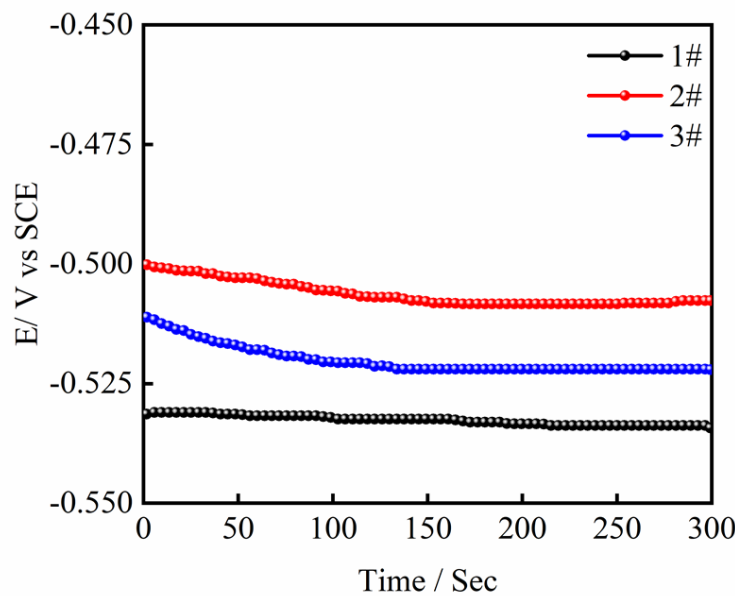
Figure 3. The open circuit potential of the samples with different thermal inputs in 3.5 wt.% NaCl solution at 25 ± 1°C.

Open circuit potential is the electrode potential when the current density is zero. That is, the potential difference between the working electrode and the reference electrode without any load. The value indicates the corrosion resistance of metals in a corrosive environment [20]. The open circuit potential (OCP) is presented in Figure 3. The results show that sample 2# has the highest open circuit potential (- 0.5071 V), which indicates that it may have the best corrosion resistance [21]. The open circuit potential of sample 3 is -0.5216 V and that of sample 1 is -0.5447 V. This turned out to be the case, as indicated by the corrosion resistance of sample 1#, which is lower than that of sample 2# and higher than that of sample 1#.

The electrochemical properties were further analyzed by electrochemical impedance spectroscopy (EIS). EIS is a test method that adds a sinusoidal potential wave with a different frequency and a small amplitude to the electrochemical system, so that it follows the change of the sine wave over time. The corresponding electrode potential changes with time [22]. The corrosion resistance of metals is proportional to the arc radius. The larger the capacitance arc radius, the greater the corrosion resistance of the metal. The results are depicted in Figure 4. The results show sample 2# has the largest capacitive reactance arc radius, indicating that this sample has the best corrosion resistance. The capacitive reactance arc radius of sample 1# is the smallest, while that of sample 2 # and sample 3# is similar, which is 2 - 3 orders of magnitude larger than that of sample 1#. The capacitive reactance arc radius of sample 2 # is also larger than that of sample 3#. The impedance is consistent with the precipitation of carbides in metallographic structures. The more that precipitates, the lower the impedance [23]. It is also important to note that with the increase of heat input, the corrosion resistance of the deposited metal decreases gradually.
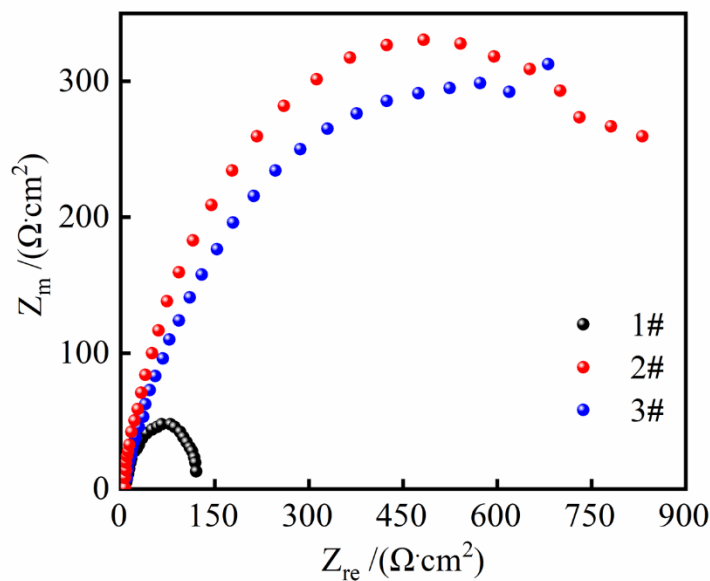
Figure 4. EIS of samples with different thermal inputs (the AC excitation signal is 1 mV/s with 25 ± 1°C)
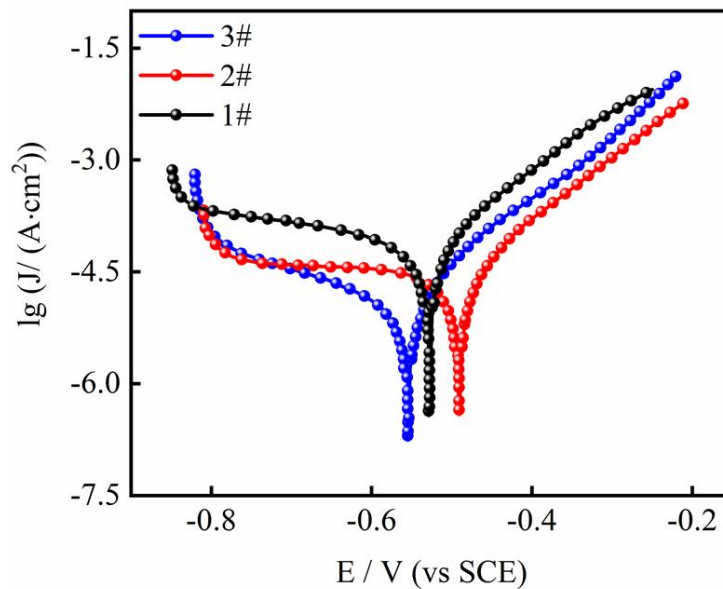
Figure 5. Potentiodynamic polarization curves (scanning rate: -1 mV/s) of the samples with different thermal inputs in 3.5 wt.% NaCl solution at 25 ± 1°C.

The polarization curves of different thermal inputs are shown in Figure 5. The corrosion potential E_{corr} and corrosion current density J_{corr} were measured by the Tafel curve extrapolation method. A higher corrosion potential indicates smaller corrosion tendency, and lower corrosion current density means slower corrosion efficiency. From -0.8V to E_{corr}, the sample is in the cathode region, and the current density decreases slowly with the increase in potential. When the potential exceeds E_{corr} (E_{corr} to - 0.2V), the current density increases with the increase in potential. The results of corrosion potential and corrosion current density are reported in Table 2. The sample 2# has a higher corrosion potential (–0.491 V), which indicates that the corrosion is less prone than the other two curves. On the other hand, the corrosion current value of sample 2# (0.000378 µA • cm^2) is only one-thirty-eighth and one-seventh times of that of sample 1# and 3#, respectively, which indicates that the corrosion rate of 2# is lower than that of the other two. The above analysis shows that the polarization curve of 2# has a higher corrosion potential, a slower corrosion rate, and therefore, has the best corrosion resistance.

Table 2. Electrochemical parameters obtained from polarization curves

| Parameters	1#	2#	3#
J_{corr} (µA • cm^2)	0.0142	0.000378	0.0278
E_{corr} (V)	-0.528	-0.491	-0.584

3.3 Corrosion resistance of surfacing layer

The effect of microstructure on the electrochemical changes was investigated by SVET. The results illustrated in Figure 6 are the area away from the fusion line in the specimen. It can be seen from

the figure that the corrosion current tends to decrease, and this region shows the characteristics of the cathode. The cause for this is attributed to the influence of the welding thermal cycle. The deposited metal is diluted by the base metal. Its alloy element content is lower than that of the top metal of the surfacing layer, and the corrosion resistance of the fusion line is obviously lower than that of the top metal.

The relationship between the structure and the corrosion resistance was thoroughly analyzed. The microstructure of sample 1# is shown in Figure 6 (a-Ⅰ, a-Ⅱ, and a-Ⅲ). The results indicate that this would lead to an increase of corrosion current density because of a large number of tungsten carbide particles, which were randomly deposited near the fusion line. The maximum current density value and average value reached were 2.2 mA/cm^2 and 0.819619 mA/cm^2, respectively. Among the above cases, a reason for the lower corrosion resistance could be due to the lower content of the Cr and W elements.

The microstructure of sample 2# is shown in Figure 6 (b-Ⅰ, b-Ⅱ, b-Ⅲ). With the increase of thermal inputs, tungsten carbide particles partially melt and the W element enters into the matrix as a solid solution element, which improves the corrosion resistance of the matrix. The maximum value and average value of 2# reached was 0.00162 mA/cm^2 and -0.001572 mA/cm^2, respectively. Interestingly, the solid solution W element combines with the Fe and C elements, and precipitates W_2C, Fe_3W_3F, Fe_4W_2C, Fe_6W_6C, and other intermetallic compounds after further increasing the thermal input. The maximum value and average value of sample 3# reached 0.0027 mA/cm^2 and -0.000071 mA/cm^2, respectively. In summary, corrosion resistance increases first and then decreases with the increasing thermal inputs, with sample 2# exhibiting optimal corrosion resistance.
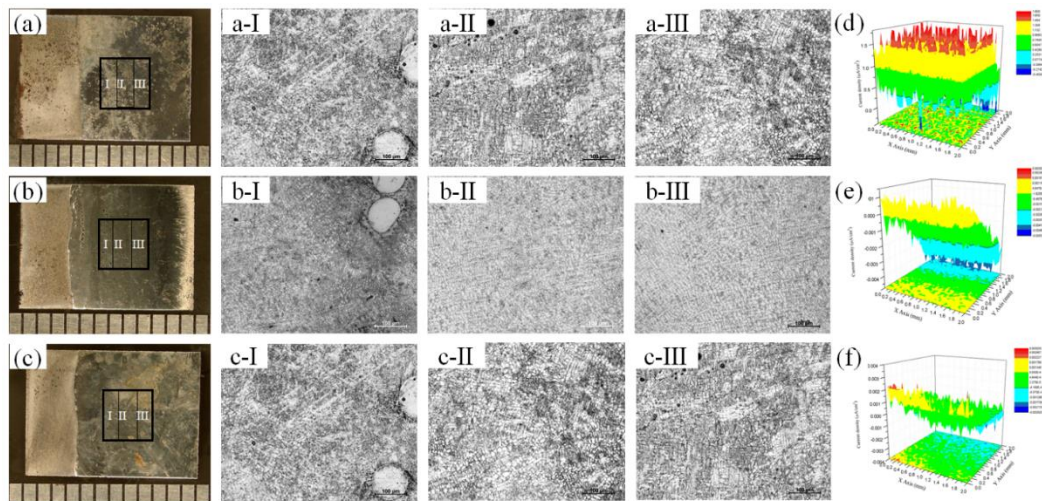
Figure 6. SVET analysis of the microstructure of the surface layer near the fusion line. (a) Macro morphology of the sample 1# cross section; (a-Ⅰ, a-Ⅱ and a-Ⅲ) the OM of the Ⅰ, Ⅱ and Ⅲ regions in 1#; (b) macro morphology of the sample 2# cross section; (b-Ⅰ, b-Ⅱ and b-Ⅲ) the OM of the Ⅰ, Ⅱ and Ⅲ regions in 2#; (c) macro morphology of the sample 3# cross section; (c-Ⅰ, c-Ⅱ and c-Ⅲ) the OM of the Ⅰ, Ⅱ and Ⅲ regions in 3#; (d)~(f) the three-dimensional SVET analysis of 1#, 2# and 3#, respectively.
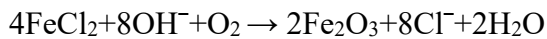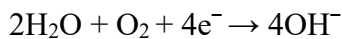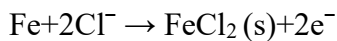
In addition, the corrosion morphology after an electrochemical test is presented in Figure 7. The result shows that there are more corrosion products and obvious corrosion pits in the vicinity of the fusion line of sample 1#. In contrast, the corrosion products of sample 2# is lower than that of the other samples and also shows a metallic luster. This result is consistent with the expected electrochemical performance.
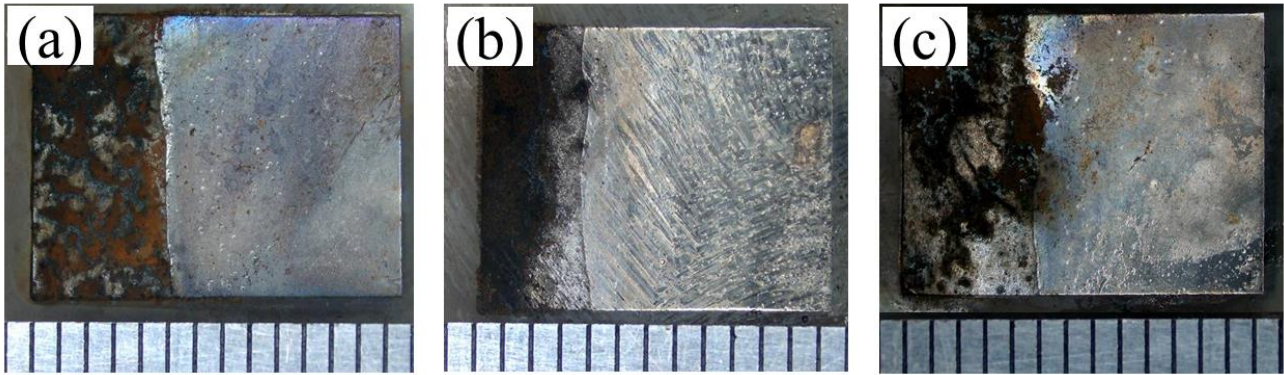
Figure 7. Corrosion morphology after the electrochemical test on samples with different thermal inputs (a) 1# (b) 2# and (c) 3#

It is generally known that a series of corrosion reactions occur in the surface layer in aqueous solution [24]:

$$Fe + 2Cl^- \rightarrow FeCl_2\,(s) + 2e^-$$
$$2H_2O + O_2 + 4e^- \rightarrow 4OH^-$$
$$4FeCl_2 + 8OH^- + O_2 \rightarrow 2Fe_2O_3 + 8Cl^- + 2H_2O$$

Because the content of Cr, Mo, V and other alloy elements in the high-chromium matrix are not enough to affect the formation of a stable passive film, the corrosion resistance of a high-chromium system is mainly affected by the size and quantity of carbides. With the increase of carbide content, the content of Cr, Mo, and other alloy elements that are conducive to the formation of a stable passive film in the matrix decreases, resulting in a decrease in corrosion resistance [25]. Furthermore, local corrosion galvanic cells are formed by the segregation of components, and the precipitation of carbides along grain boundaries [26]. The change of thermal input directly affects the melting behavior and carbide distribution of WC in the surfacing layer, which then changes the corrosion resistance [27]. Therefore, regulating the thermal input represents an appealing and effective means by which to improve the corrosion resistance of high-chromium wear-resistant steel.

4. CONCLUSIONS

In this study, the effect of microstructure and corrosion resistance in the WC-particle-reinforced high-chromium wear-resistant steel by thermal inputs was studied. The results show that sample 2# displays the highest corrosion potential (-0.491 V) and the lowest corrosion current density (3.78×10^{-4}

$\mu A \cdot cm^2$) of all the conditions tested. The SVET results and microstructure analyses imply that the reasonably well thermal inputs can provide efficient element distribution and promote the dissolution of the WC phase. The change of thermal input directly affects the melting and carbide distribution of WC in the surface layer, which then changes the corrosion resistance. This work provides a reference for improving the corrosion resistance of high-chromium wear-resistant steel.

References

1. X. Yin, J. Jin, X. Chen, A. Rosenkranz, J. B. Luo, *ACS Appl. Mater. Inter.*, 11(2019)32569.
2. C. A. Damião, G. C. Alcarria, V. C. Teles, J. D. B. D. Mello, W. M. D. Silva, *Wear.*, 426(2019)101.
3. P. K. Farayibi, M. Blüm, S. Weber, *Mat. Sci. Eng. A-Struct.*, 777(2020)139053.
4. L. Huang, X. Deng, C. R. Li, Y. Jia, Q. Wang, Z. D. Wang, *Wear.*, 434(2019)202971.
5. Y. M. Kuskov, V. A. Zhdanov, I. O. Ryabtsev, M. M. Student and H. H. Veselivska, *Mater. Sci.*, 55(2020)710.
6. R. P. Garcia, S. C. Canobre, H. L. Costa, *Tribol. Int.*,143(2020)106080.
7. J. Yao, Y. Ding, R. Liu, Q. L. Zhang, L. Wang, *Opt. Laser Technol.*, 107(2018)32.
8. S. Viswanathan, L. Mohan, P. Bera, V. P. Kumar, H. C. Barshilia, C. Anandan, *J. Mater. Eng. Perform.*, 26(2017)3633.
9. M. R. Ripoll, N. Ojala, C. Katsich, V. Totolin, C. Tomastik, K. Hradil, *Mater. Design.*, 99(2016) 509.
10. W. Liang, *Appl. Surf. Sci.*, 211(2003)308.
11. X. Xu, Z. C, J. Wang, Z. Yu, R. Zhang, Z.Qiao, Liu, *Adv. Mater.*, 30(2018) 1702944.
12. A. Fossati, F. Borgioli, E. Galvanetto, T. Bacci, *Corros. Sci.*, 48(2006)1513.
13. X. Tang, R. D. Chung, B.Li, Hinckley, K. Dolman, *Wear.*, 267(2009)116.
14. D. Bartkowski, A. Młynarczak, A. Piasecki, B. Dudziak, M. Goscianski, A. Bartkowska, *Opt. Laser Technol.*, 68(2015)191.
15. L. Fedrizzi, S. Rossi, F. Bellei , F. Deflorian, *Wear.*, 253(2002)1173.
16. A. Dalmau, C. Richard, A. Igual–Muñoz, *Tribol. Int.*, 121(2018)167.
17. C. Yi and B. Zhu, *Int. J. Electrochem. Sci.*, 14(2019)6759.
18. Y. Javadi, N. E. Sweeney, E. Mohseni, C. N. Macleod, D. Lines, M. Vasilev, Z. Qiu, R. K. W. Vithanage, C. Mineo, T. Stratoudaki, S. G. Pierce, A. Gachagan, *Mater. Design.*, 195(2020)108981.
19. C. Park, N. Kang, S. Liu, *Corros. Sci.*, 128(2017)33.
20. J. Jung, J. Yu , J. H. Lee, *J. Phys. Chem. Lett.*, 9(2018)5412.
21. K. Charoenkitamorn, P. T. Tue, K. Kawai, O. Chailapakui, Y. Takamura, *Sensors-Basel.*, 18(2018) 444.
22. F. Ciucci, *Curr. Opin, Electroche.*, 13(2019)132.
23. Y. Zhang, Q. Cai, Y. Liu, Q. Y. Guo, H. J. Liu, *J. Mater. Eng. Perform.*, 28(2019)1892.
24. V. I. Babushkin, G. M. Matveyev, O. P. Mchedlov-Petrossyan, Corrosion Reactions,

Thermodynamics of Silicates*.*, 1985.

25. H. Ai, J. Hou, X. Ye, C. Zeng, H. Sun, X. Li, G. Yu, X. Zhou, *J.*Wang*, Nucl. Mater.*, 503(2018)116.
26. R. N. Clark, J. Searle, T. L. Martin, W. S. Walters, G. Williams, *Corros. Sci.*, 165(2020)108365.
27. H. Wang, H. Lu, X. Song, X. Yan, X. Liu, Z. Nie, *Corros. Sci.*, 147(2019)372.